UCRL-TR-206843

LAWRENCE
LIVERMORE
NATIONAL
LABORATORY

Development of a Rolling Process Design Tool for Use in Improving Hot Roll Slab Recovery

Richard Couch, Richard Becker, Moono Rhee,
Ming Li

September 27, 2004

Disclaimer

This work was performed under the auspices of the U.S. Department of Energy by University of California, Lawrence Livermore National Laboratory under Contract W-7405-Eng-48.

DEVELOPMENT OF A ROLLING PROCESS DESIGN TOOL FOR USE IN IMPROVING HOT ROLL SLAB RECOVERY

DOE Contract (Field Work Proposal) No. EEW0087
CRADA No. TC-02028

Final Report

June 1, 2001 – Aug 31, 2004

by

Richard Couch
Richard Becker
Moon Rhee

Lawrence Livermore National Laboratory
PO Box 808; L-99
Livermore, CA 94550
Phone: 925-422-1655
FAX: 925-422-3389
couch1@llnl.gov

and

Ming Li

Alcoa Incorporated
Alcoa Technical Center, ATC-B
100 Technical Drive
Alcoa Center, PA 15069
Phone: (724) 337-2492
FAX: (724) 337-2005
Ming.Li@alcoa.com

Prepared for
U.S. Department of Energy

TABLE OF CONTENTS

1. EXECUTIVE SUMMARY

Lawrence Livermore National Laboratory participated in a U. S. Department of Energy/Office of Industrial Technology sponsored research project "Development of a Rolling Process Design Tool for Use in Improving Hot Roll Slab Recovery", as a Cooperative Agreement TC-02028 with the Alcoa Technical Center (ATC).

The objective of the joint project with Alcoa is to develop a numerical modeling capability to optimize the hot rolling process used to produce aluminum plate. Product lost in the rolling process and subsequent recycling, wastes resources consumed in the energy-intensive steps of remelting and reprocessing the ingot. The modeling capability developed by project partners will be used to produce plate more efficiently and with reduced product loss. Major objectives of this project were identified in the statement of work in the proposal as:

- Predict temperature, stress, strain, strain rate history and damage evolution of slab material as it evolves through multi-pass rolling
- Determine the effect of initial slab shape and rolling pass schedule on fracture and internal product integrity
- Demonstrate the utility of numerical model as a forming process optimization tool

In accomplishing these objectives, eight subtasks were identified as:

1. *Determine material constitutive properties.*
2. *Determine material fracture properties.*
3. *Implement friction model.*
4. *Characterize the hot rolling process by determining boundary and initial conditions.*
5. *Produce rolling data for code validation*
6. *Validate finite element model.*
7. *Apply model to production rolling configuration.*
8. *Perform parameter studies by evaluating temperature distribution, roll speed, ingot geometry, pass schedule and roll gap geometry.*

Based on project findings and availability of appropriate data, several of these tasks were modified. In the end, the model developed successfully captured the thermo-mechanical history, shape change and center fracture observed in laboratory rolling experiments. It also successfully predicted side roll over and demonstrated effects of friction on production mill geometry. The code was delivered to Alcoa Technical Center for their internal use.

2. BACKGROUND

Aluminum plate is produced by rolling a hot slab multiple passes in a reversing mill. The large deformations and stress states encountered in the slab can lead to failure modes that result in loss of the entire slab. These include the formation of defects within the plate, edge cracking, plate delamination, alligatoring (center splitting of the slab near the front and rear end), and the formation of undesirable rolled end shapes. In addition to resultant plant-associated inefficiencies related to processing material that does not yield a sellable product, the slab material that does not result in useful product must be reprocessed to form fresh ingot material. Further, there is also equipment downtime associated with several of the failure modes.

Significant improvements in energy efficiency can be attained if the slab material response to the hot rolling process was sufficiently well understood that processing parameters could be chosen that minimize loss of product. Currently, processing parameters are optimized by trial and error or by approximate models. Numerical simulation of the full thermal-mechanical process could play a major role in optimizing the process and increasing product yield.

This project was structured to take greatest advantage of the strengths of LLNL and of Alcoa's Technical Center (ATC). Alcoa provided the experience in aluminum processing and the ability to provide the data required to develop numerical process models and material constitutive models. LLNL provided the experience in performing large, complex, three-dimensional numerical simulations of thermal-mechanical systems, and experience in material constitutive and fracture models. LLNL was responsible for producing finite element models of the hot rolling process and the slab material response. Alcoa generated and provided the processing and material characterization data required to validate the numerical models. Alcoa, as a major supplier of aluminum flat rolled products, will utilize the knowledge gained and the numerical tools developed to reduce energy consumption, and it will propagate the resultant gains from an optimized hot rolling process to other process.

2.1. Technical Accomplishments

There are two fundamental concepts assumed in applying the modeling strategy. The first is that given an aluminum alloy, a well defined series of characterization measurements are sufficient to create a description of material behavior that can be used in a numerical simulation of the hot rolling deformation process. The second concept is the assumption that, given a physical description of the hot rolling process and given the material properties of the aluminum slab, a numerical simulation can be used to predict the response of the material, including damage evolution, after multiple roll passes.

The following measurements and characterizations were performed to provide data for the modeling efforts.

- Determined flow strength of the slab alloy as a function of strain, strain rate and temperature.
- Determined a fracture model that defines a failure surface in stress-strain-strain rate-temperature space.
- Evaluated fracture mechanisms by examining the mictrostructure at the fracture surfaces.

The computational model of the rolling process and slab material response require:

- The physical configuration of the roll/slab process and its associated initial and boundary conditions were represented in a finite element model.
- The representation of the alloy material response was validated by reproducing the results of the curve fits made above to define the material properties.
- A model for the fracture response of the alloy was created and implemented in the simulation code.
- Numerical simulations were conducted to reproduce observed deformation characteristics produced by roll passes.

These are complex three-dimensional multi-physics simulations that have not previously been accomplished in studies of multi pass hot rolling.

2.2 Technical Progress Against Plan

Task schedule by program quarter:

1.	Determine material constitutive properties:	Q1->Q3
2.	Determine material fracture properties:	Q2->Q5
3.	Develop friction model:	Q2->Q3
4.	Characterize hot rolling process: boundary and initial conditions;	Q1->Q3
5.	Produce rolling data for code validation:	Q5->Q6
6.	Finite element model validation:	Q3->Q8
7.	Apply model to production rolling configuration:	Q9->Q10
8.	Perform parameter studies:	Q10->Q12

The project was initiated in July of 2001 with completion in August 2004. All major tasks were completed on time with minor sub task delays due to technical issues involved with the parallel thermal algorithms in the finite element code.

ATC was responsible for providing the physical parameters required to model the rolling process and the data required for code validation. This data includes the material characteristics and model parameters necessary to describe the aluminum alloy, the characterization of the properties of the deformed slab material at several stages in the rolling process, and a description of the failure characteristics of the alloy as a function of deformation, which will be described in Section 3.1.

LLNL was responsible for numerical model development in support of the hot rolling simulations, and for the simulations required to verify and to validate the models. This also included the development of appropriate boundary conditions to represent the physical features associated with the hot rolling process. Numerical modeling approach is discussed in Section 3.2.

3. RESULTS

3.1. EXPERIMENTAL

Aluminum-Magnesium alloys are some of the most widely used non-heat treatable alloys due to their high strength, good formability, high levels of corrosion resistance and weldability. The role of Mg additions in strengthening Al-Mg alloys has been well characterized in the literature [1]. It is also well known that fabrication difficulties of high-Mg aluminum alloys, mainly associated with hot fracture behavior, have severely limited the applications of Mg containing alloys. Nevertheless, new developments in casting technology and advanced control of thermo-mechanical processing could revive interest in increasing Mg content to further strengthen Al-Mg alloys.

A fundamental understanding of hot fracture behavior thus becomes a key to improving manufacturability of Al-Mg alloys in industrial processes, and in developing new Al-Mg alloys, processes and products. In the past, focus was placed on ductile fracture as one of the dominant fracture mechanisms for metals with high ductility, particularly for aluminum alloys processed at room and elevated temperatures. According to Ashby's fracture mechanism maps for FCC alloys [2], there are several fracture mechanisms operating in a range of elevated temperatures and tensile stresses (corresponding strain rates). Therefore, there is a need to address multiple fracture modes when developing criteria to characterize hot fracture behavior during thermo-mechanical processing.

Tension tests conducted at high temperatures are used to determine the constitutive response and the strain to fracture for three different Al-Mg alloys at various temperatures and strain rates. Multiple fracture modes are identified by experimental observations and microstructure examinations. A ductile fracture criterion capturing multiple fracture mechanisms at elevated temperature is proposed. The model and its application to rolling simulation are discussed in section 3.2.

3.1.1 Material

Three types of Al-Mg 5XXX aluminum alloys, referred to as alloy 1, alloy 2, and alloy 3 were chosen for fracture evaluation. Alloys 1 and 2 were received as cast and alloy 3 was partially hot rolled. The materials were supplied by an Alcoa plant. The chemical composition of the alloys is given in Table I, where the Mg level is distinguished by low and high levels. Also notable is that Alloys 2 and 3 are similar in chemical composition but have different processing histories.

Table I Chemical Composition of Al-Mg Alloys.

Alloy	Mg	Mn	Cu	Ti	Other	Process
1	Low	0.24	0.024	0.0105	Fe+Si 0.42 max	As-cast
2	High	0.34	0.04	~0.005	Fe+Si 0.41 max	As-cast
3	High	0.34	0.06	~0.005	Fe+Si 0.45 max	Partially rolled

The as-cast specimens were homogenized with a 12 hour log heatup to 0.83 T_M , soaked for four hours at 0.83 T_M and air cooled. T_M is the melting temperature of the specific alloy.

3.1.2 Tensile Tests

Tensile specimens were fabricated from slabs in the through-thickness direction. The orientation is such that strength and ductility of materials in the thickness direction can be measured. The dimensions of the tensile specimens (0.225 in. diameter and 1.24 in. gauge length) are illustrated in Figure 1. A thermocouple inserted in the end of the tensile specimen is used to control the temperature prior to the test. The apparatus used to conduct the tensile tests in a compression load frame is represented schematically in Figure 2. It is composed of two parts which slide relative to each other when subjected to compressive motion of the ram. The tensile specimens are threaded to each part.

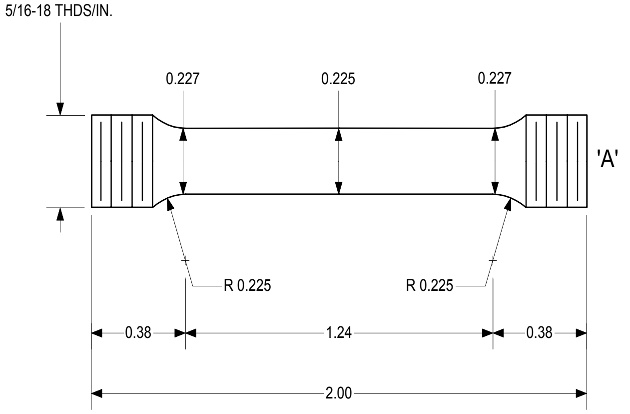

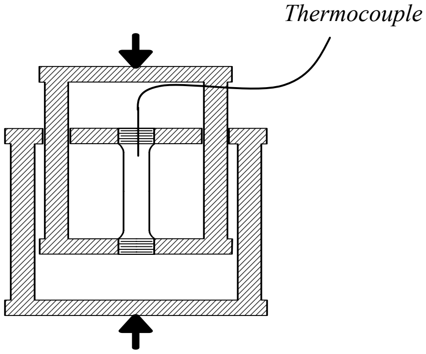

Figure 1. Dimension of the tensile specimen.

Figure 2. Schematic of the tensile apparatus for elevated temperature testing.

The cylindrical samples were deformed in uniaxial tensile stress at isothermal and constant true strain rate conditions using a servo-hydraulic controlled tester. The control of true strain rate is based on real time calculation of the ram velocity divided by the current gauge length. Assuming the tensile stretch is uniform throughout the gauge length, the logarithmic tensile strain is calculated in a real time. The change of cross section area of the tensile specimen is determined assuming constant volume, and the true stress calculated.

The test procedure was to heat the specimen to temperature, hold for 30 sec and pull to failure at a constant strain rate. High temperature tensile tests were performed at four temperatures (0.79 T_M , 0.82 T_M , 0.85 T_M and 0.88 T_M) and under two strain rates (0.3 and $3.0\sec^{-1}$).

Typical deformed and fractured tensile specimen are depicted in Figure 3. A small amount of necking observed.

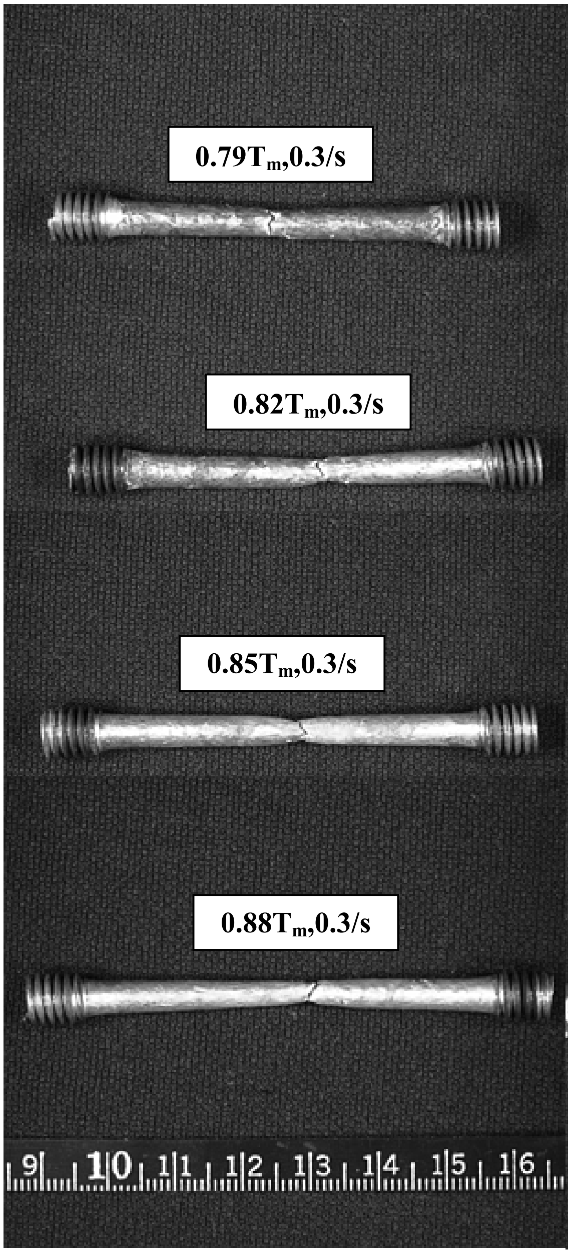

Figure 3a. Alloy 1, deformed at low strain rate.

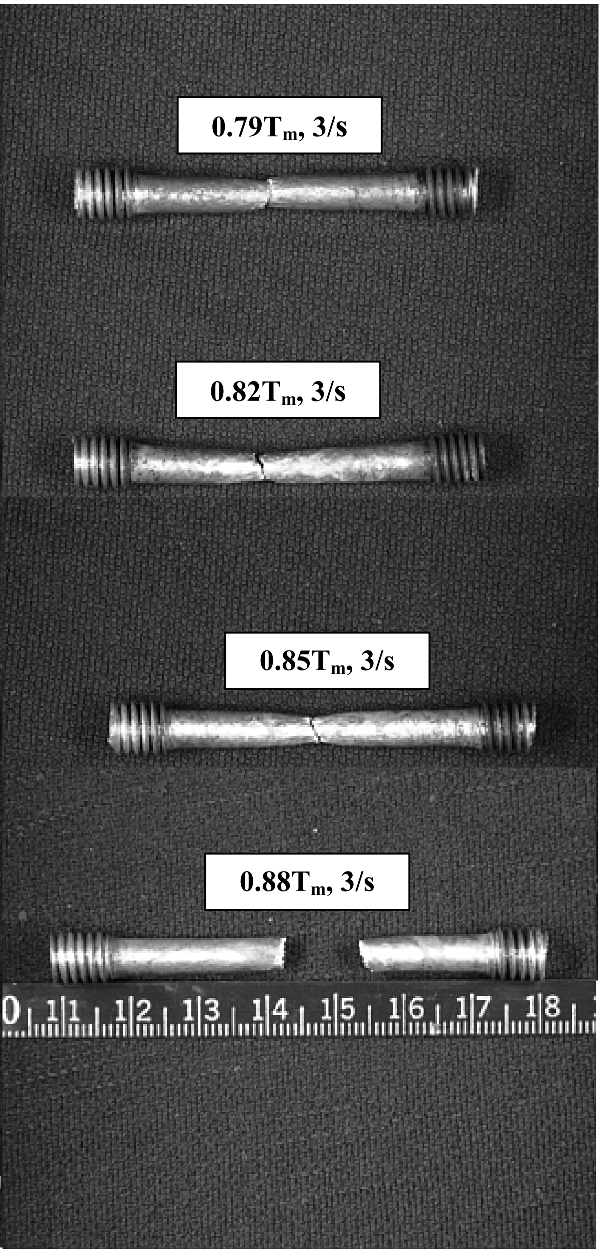

Figure 3b. Alloy 1, deformed at high strain rate.

3.1.3 Test Results and Constitutive Models

True stress and strain were determined under the assumption that the specimen was uniformly deformed across the gauge length. In these elevated temperature tests, the high rate sensitivity stabilizes the deformation and localized necking is delayed considerably. Even at fracture figure 3, necking is very diffuse. In selecting data for fitting the stress-strain curves, all data up to the rapid stress drop associated with incident fracture were used. The strain to fracture obtained from the tensile stress-strain curves is determined at the strain level close to the beginning of the rapid stress drop.

The stress-strain curves and the point designated as the fracture strain are depicted in Figures 4 - 6 for alloys 1, 2 and 3, respectively. In each figure, frame “a” is the low strain rate response and “b” is the high strain rate response. There were duplicate specimens for nearly all testing conditions. The ‘data point’ on each curve is the location representing the strain where incipient fracture is assumed. It is located at the midpoint of the knee where the state of stress starts to change rapidly. The stress determined in that region will not be reliable due to necking. The spikes or ‘ringing’ in the low strain region of the high strain rate tests are due to dynamic responses from the feedback control loop attempting to maintain a constant strain rate. The duplicate tests show a potentially wide variability in fracture strain.

In Figures 4a and 4b, tensile responses of as-cast alloy 1 show that at the lower strain rate (0.3 per second), the flow stress decreases and the tensile fracture strain increases with an increase of deformation temperature. However, at the high strain rate (3.0 per second), the tensile fracture strain does not increase with temperature.

In Figures 5a and 5b, tensile responses of as-cast alloy 2 show that the flow stress decreases with the increase of deformation temperature for both low and high strain rate cases. The fracture strain generally increases with temperature at the lower strain rate until the deformation temperature reaches a transition range of $0.85 T_M$ to $0.88 T_M$. In this transition range, the fracture strain drops rapidly from 0.25 to 0.06 approximately. For the higher strain rate, the transition range appears to happen earlier, from $0.82 T_M$ to $0.85 T_M$. This is an interesting observation that the maximum strain (defined as fracture strain or hot ductility) may not be monotonic in temperature.

The tensile responses of alloy 3 depicted in Figures 6a and 6b. Again, we observed a temperature transition zone where the ductility may be decreased. At the lower strain rate, it is near $0.88 T_M$ and at the higher strain rate, it is between $0.85 T_M$ to $0.88 T_M$.

For hot working conditions, material constitutive models describing the flow strength response may use as a functional form composed of internal state variables and externally applied variables. Internal state variable theories proposed by Sample et al [3] for fully dense materials and later extended by Wang et al [4] for materials containing voids are briefly described here. In general, internal variables are intended to represent the state of microstructure, i.e., microhardness, dislocation density, void morphology, etc.

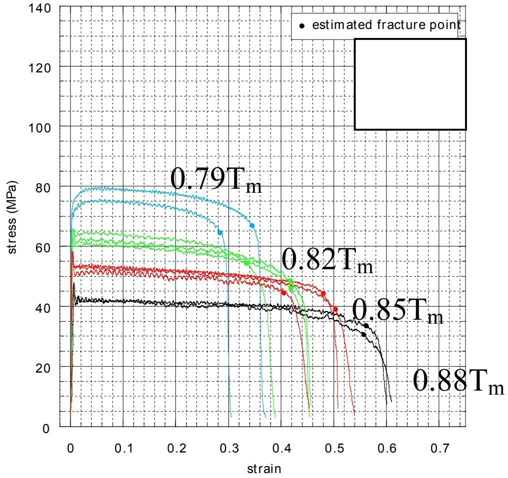

Figure 4a. Stress-strain curves of Alloy 1 under 0.3/s.

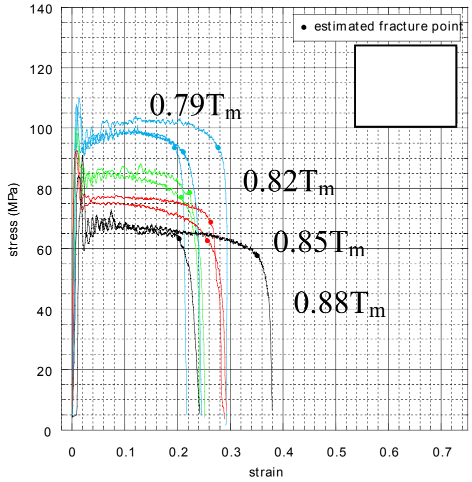

Figure 4b. Stress-strain curves of Alloy 1 under 3.0/s.

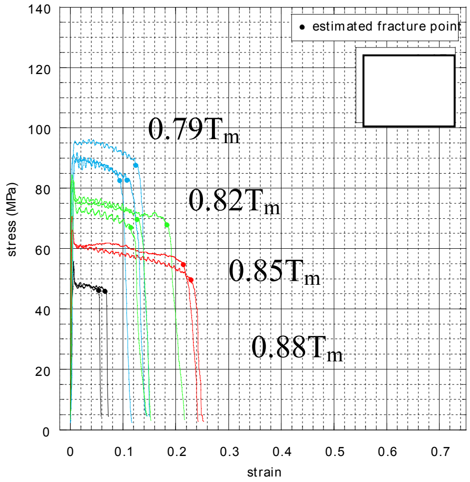

Figure 5a. Stress-strain curves of Alloy 2 under 0.3/s.

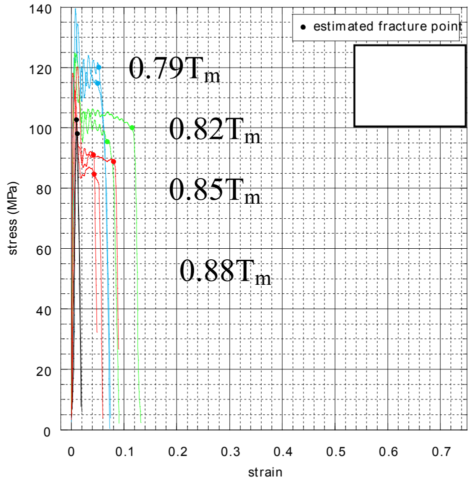

Figure 5b. Stress-strain curves of Alloy 1 under 3.0/s.

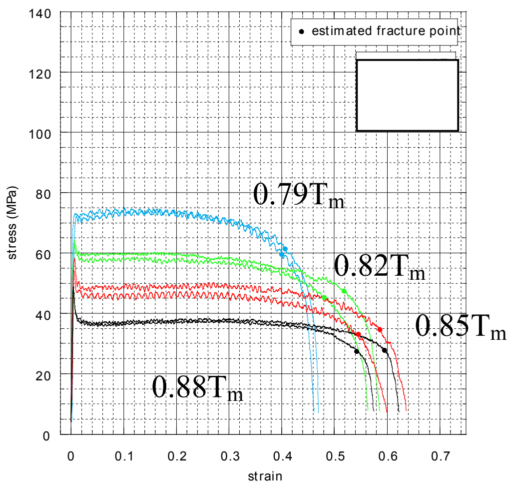

Figure 6a. Stress-strain curves of Alloy 3 under 0.3/s.

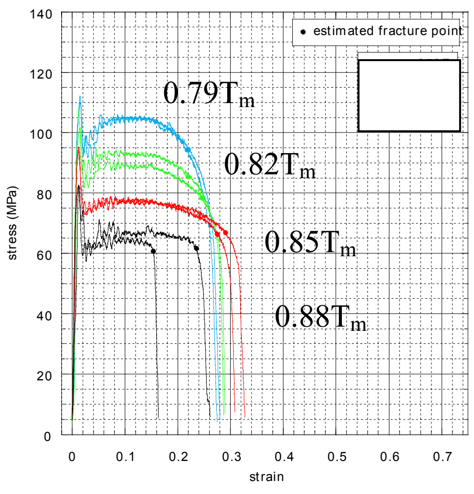

Figure 6b. Stress-strain curves of Alloy 1 under 3.0/s.

The strain rate and temperature effects on the flow stress are important for elevated-temperature deformation processing. The flow stress ($\bar{\sigma}$) and internal state variables evolution rates $\left(\dot{S}^r\right)$ are schematically represented as

$$\bar{\sigma} = g(\dot{\varepsilon}, T, S^r, C^r) \tag{1}$$

$$\dot{S}r = hr(\dot{\varepsilon}, T, Sr, Cr), \tag{2}$$

which depend on process variables such as strain rate $\left(\dot{\varepsilon}\right)$ and temperature (T), the internal state variables $\left(\dot{S}^r\right)$, and the composition $\left(C^r\right)$.

From the data represented in Figure 4-6 it is evident that the flow stress reaches a saturation value very quickly. To simplify the constitutive model, only the saturated stress $\bar{\sigma}^*$ as a function of temperature and strain rate is determined for these Al-Mg alloys. The saturated flow stress was estimated prior to fracture in Figures 4 - 6 by assuming a constant value independent of strain. At high temperatures and constant composition, the saturated stress $\bar{\sigma}^*$ as a function of temperature and strain rate fit to the form

$$\bar{\sigma}^* = \frac{1}{\alpha}\sinh^{-1}\left[\left(\frac{Z}{A}\right)^{1/n}\right], \tag{3}$$

where

$$Z = \dot{\varepsilon}\exp\left(\frac{Q}{RT}\right). \tag{4}$$

Z is the temperature compensated strain rate (Zener-Hollomon parameter), Q the activation energy, R the gas constant and T the absolute temperature. The material constants for the three materials are listed in Table II. The saturated flow stress plotted against *Ln(Z)* is depicted in Figure 7.

Table II Material Constants of the Constitutive Model.

Constant	Alloy 1	Alloy 2	Alloy 3
α (MPa^{-1})	0.04002	0.02835	0.02689
n	2.320	2.826	2.697
ln A (sec^{-1})	20.43	23.90	20.04
Q (J/mole)	251000	283200	229600

3.1.4 Material Fracture Properties

The hot fracture behavior of the Al-Mg alloys was evaluated under simplified lab testing conditions. Two fracture modes – ductile fracture and hot shortness – were observed at temperatures in the range of 0.75 T_m to 0.9 T_m and strain rates from 0.3 to 3.0/s. These two fracture modes were detected by the analysis of hot tensile fracture data and by detailed SEM evaluation. For ductile fracture, the fracture strain increases with increasing deformation temperature or decreasing strain rate, and it is correlated with the Zener-Hollomon parameter. For the hot shortness mode, temperature and strain rate are related to fracture in a different way. A multiple-mode fracture criterion was created based on experimental data from tensile tests. It has the potential to describe both ductile fracture and hot shortness modes in a thermomechanical processing region. Additional tests may be required to fine-tune the formulations. Nevertheless, the model was applied in a hot rolling simulation to assess the model response.

The equivalent strain to fracture, $\bar{\varepsilon}_f$, determined from Figure 4 to 6 as a function of temperature and strain rate, is shown in Figure 8. It illustrates that; (1) fracture strain increases with increasing temperature until it reaches a critical temperature range; (2) fracture strain decreases with increasing strain rate for all three alloys. At this point, it must be recognized that the increase and decrease of hot ductility might relate to different fracture modes – we name them as ductile fracture and hot shortness modes respectively. Figure 8 also reveals the facts that fracture strain decreases with the increase of Mg content, and increases from as-cast to partially rolled states.

Assuming it is indeed the case that failure of Al-Mg could occur under two different fracture modes when processed at elevated temperature, we may summarize the fracture data of these three alloys as follows. For Alloy 1, the hot shortness mode begins between 0.85 T_M and 0.88 T_M at 3.0/s, and it is not evident at the lower strain rate where fracture occurs in a ductile mode. For Alloy 2, the hot shortness mode starts between 0.82 T_M and .85 T_M at 3.0/s while at the lower strain rate it occurs somewhere between 0.85 T_M and 0.88 T_M. The hot shortness behavior for alloy 3 is similar to that for alloy 2, although it occurs at a higher temperature range. Therefore, both temperature and strain rate may dictate the transition of fracture modes from ductile fracture to hot shortness.

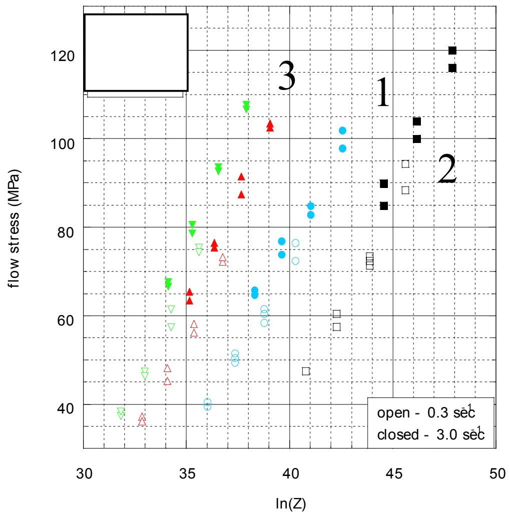

Figure 7. Saturated flow stress as a function of Zener Holloman parameter, *Ln(Z)*.

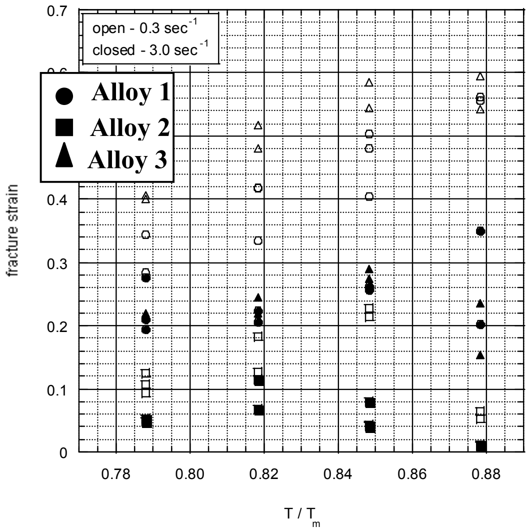

Figure8. Fracture strain as a function of temperature, strain rate, and alloy.

To further examine the fracture data, the fracture strain is plotted against *Ln(Z)* (Eq. 4) in Figure 9. The data appear rather scattered until the points assumed to be associated with the hot shortness mode are removed from the plot. The remaining points should be considered as a set of ductile fracture data. These are shown in Figure 10. It can be seen that the fracture strain for the ductile mode collapses nicely with the Zener-Hollomon parameter, *Ln(Z)*, for these three Al-Mg alloys. There is a slight variability from Alloy 3 at the high strain rate.

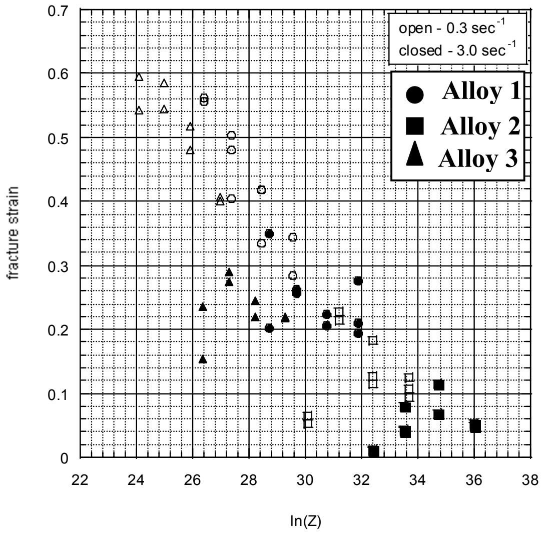

Figure 9. Fracture strain as a function of *Ln(Z)*.

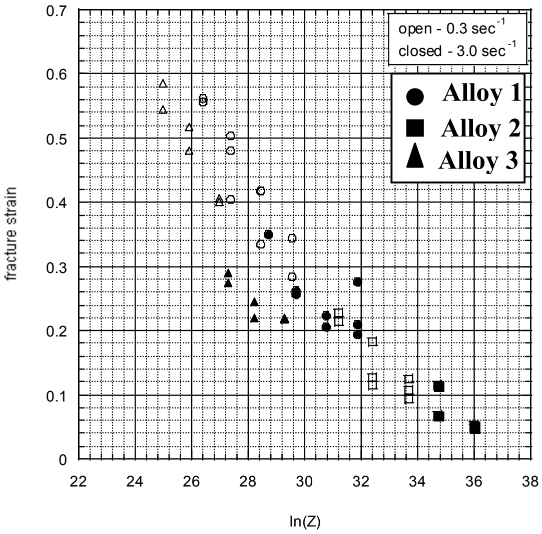

Figure 10. Fracture strain without hot shortness data.

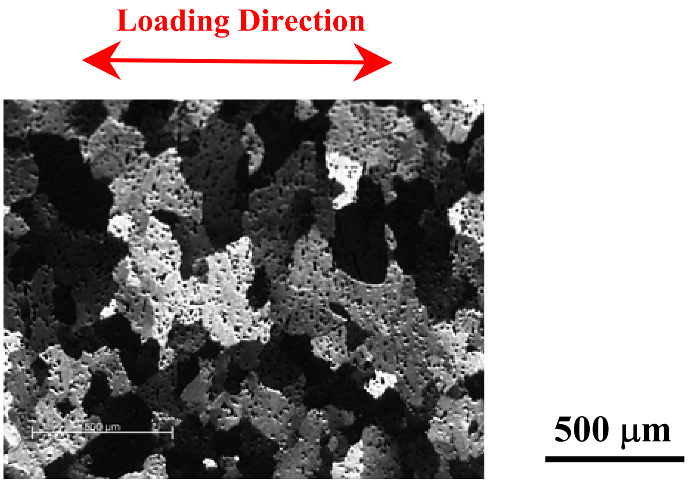

(a) Undeformed

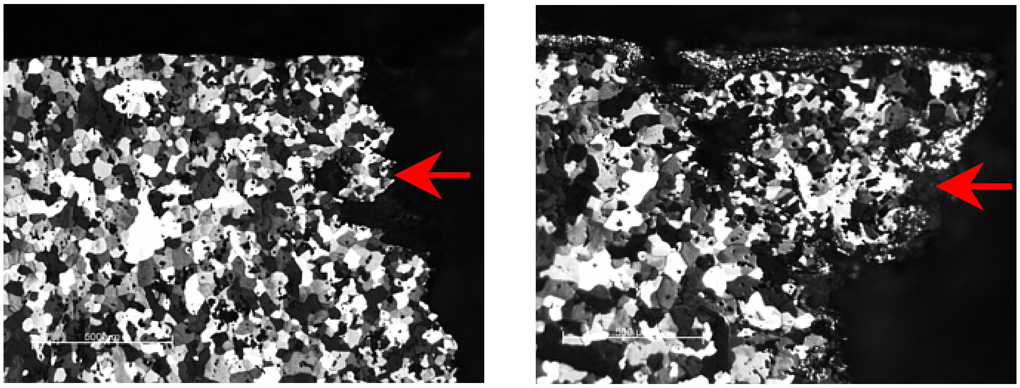

(b) 0.79T$_{m}$, 0.3/s (c)) 0.79T$_{m}$, 3/s

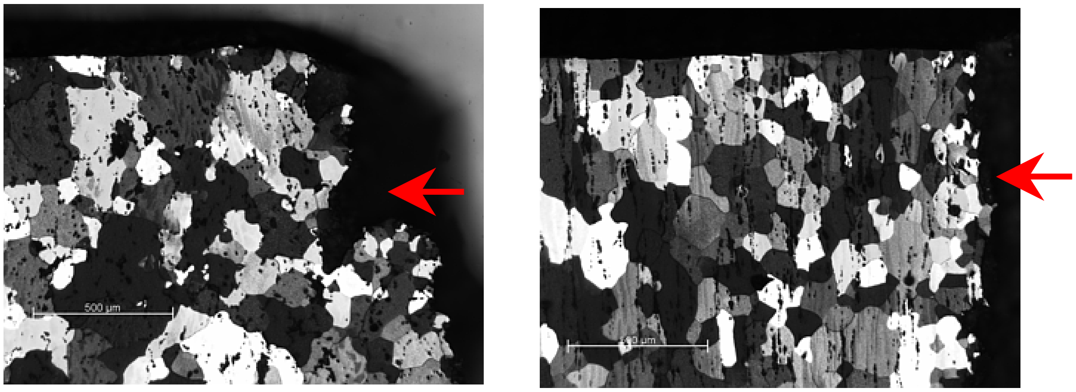

(d) 0.88T$_{m}$, 0.3/s (e) 0.88T$_{m}$, 3/s

Figure 11. Grain structures observed in the deformed tensile samples of Alloy 3. Samples were pulled in the horizontal direction in the figure. Arrows indicate the fracture surfaces of tested samples. (a) undeformed starting grain structure, (b)

deformed at 0.79 T_M and 0.3/s, (c) deformed at 0.79 T_M and 3/s, (d) deformed at 0.88 T_M and 0.3/s, (e) deformed at 0.88 T_M and 3/s.

To confirm the fracture modes discussed above, typical fracture samples representing these three alloys were examined by optical metallography and FEG-SEM. Samples from Alloy 3 were used for illustration. For optical viewing, the specimens were cut in the center along the longitudinal direction containing the applied loading direction, which was also the through-thickness direction of slabs. The samples were mounted, polished and then etched for grain structure observation.
Typical grain structures of Alloy 3, before and after hot deformation, are depicted in Figure 11 above. The un-deformed grain structure was taken from the threaded part of the sample (see Figure 1) where no deformation occurred. The deformed grain structures were taken near the fracture surface (indicated by arrow) of the deformed sample. The grain size of alloy 3 is about 200 microns for as-rolled condition while the as-cast grain size of Alloys 1 and 2 are about 450 microns. In the deformed region near the fracture surface (Figure 11 b to e), there are patches of recrystallized grains. The progression of grain refinement due to recrystallization increases with the decrease of deformation temperature, and is slightly influenced by strain rate. Moreover, the refinement of grains varies along the gauge length and appears finer when closer to the fracture surface. This may be due to local deformation when necking occurred. Thus, the variation of grain size and recrystallization add additional complexity to fracture study

SEM images of fracture surfaces of Alloy 3 samples are shown in Figure 12 for two temperatures (0.79T_m and 0.88T_m) and two strain rate conditions. In Figures 12 a and b, the depth of dimples and ridges of grain boundary are visible throughout the fracture surface where a typical shear failure observed. The depth of dimples becomes less significant in Figures 12c and 12d, where small wavy features appear on the latter surface. The trace of brittle type failure through grain boundary becomes more visible in the latter figures. It is believed that a transition from transgranular to intergranular failure might take place in Figures 11c to 11d as a result of two distinct fracture modes processing from a to d. The transgranular failure shown in Figures a and b should relate to the ductile fracture mode when shear failure is dominant. The intergranular failure shown in Figure d might be associated with the hot shortness mode by which weak links were induced along grain boundary. It is worth mentioning that some of the wavy surface features seen in c and d in the figures could be the failure sites along recrystallized grain boundaries.

Additional optical metallography results show that there are more voids at the ductile fracture surface than the hot shortness surface. It is believed that void nucleation and growth may take place uniformly across the matrix and grain boundary for the ductile fracture mode while localized failure caused by grain boundary weakness may be associated with the shot shortness mode.

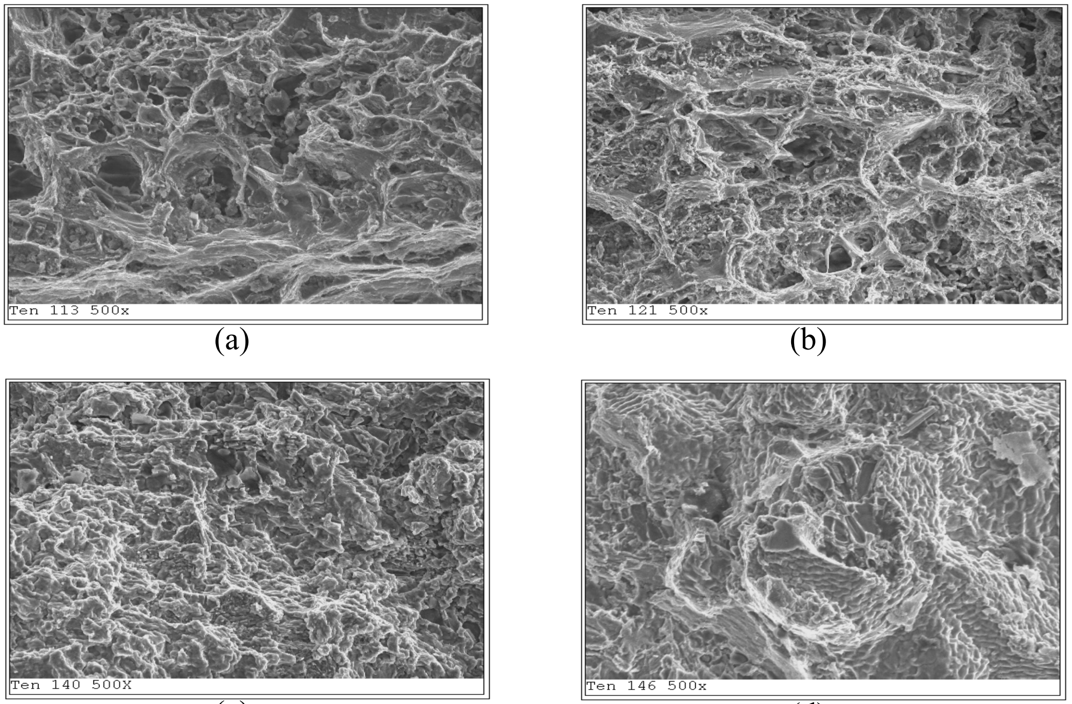

(a) (b)

(c) (d)

Figure 12. Fracture surface of Alloy 3 tensile samples deformed at (a) at $0.79T_m$ and 0.3/s, (b) at $0.79T_m$ and 3/s, (c) at $0.88T_m$ and 0.3/s, and (d) at $0.88T_m$ and 3/s. 500x

3.1.5. Multiple Mode Fracture Criteria

In bulk forming (e.g., rolling, extrusion, forging), fracture is generally complex and three-dimensional in nature. It depends on local stress states, strain rate, temperature and microstructure features. Vujovic et al [5] developed a fracture criterion based on the concept of forming limit curves similar to those used in sheet material. Alexandrov et al [6, 7] compared the criterion to experimental results of various die upsetting experiments and found that the criterion incorporating a stress triaxiality factor was in good agreement with ductile fracture of steel at room temperature. Experimental observation and data from tensile test results of Al-Mg alloys (Figures 9, 10 and 12) have provided the opportunity of developing fracture criterion for these materials. The data are summarized as follows: Fracture behavior of Al-Mg alloys at elevated temperature could have at least two fracture modes – ductile fracture and hot shortness. Fracture strain (ductility) in the ductile fracture mode can be correlated with the temperature compensated strain rate, *Ln(Z)*.

Hot ductility may shift from the ductile fracture mode to the hot shortness mode depending on the external variables: strain rate and temperature. When staying in the hot shortness mode, ductility drops rapidly

The concept of a multiple-mode fracture criterion has emerged from the data mentioned above, as illustrated in Figure 13. The schematic shows that the strain to fracture is bounded on one side by the temperature compensated strain rate, *Ln(Z)*, as the limit curve of ductile fracture mode. The three little caps branching from the limit curve represent the other side of fracture response– the hot shortness mode, dictated by the strain rate (ξ). This schematic essentially represents a fracture limit diagram, similar to Vujovic et al [5], but with the additions of *Ln(Z)* and strain rate to capture multiple fracture modes observed in Al-Mg alloys.

Figure 13 only addresses a two-dimensional fracture limit diagram under a constant stress traiaxility – that of uniaxial tension. A third axis could be added to the diagram. This would represent the stress traiaxility factor and would require experimental data of torsion and compression tests and perhaps notched bars.

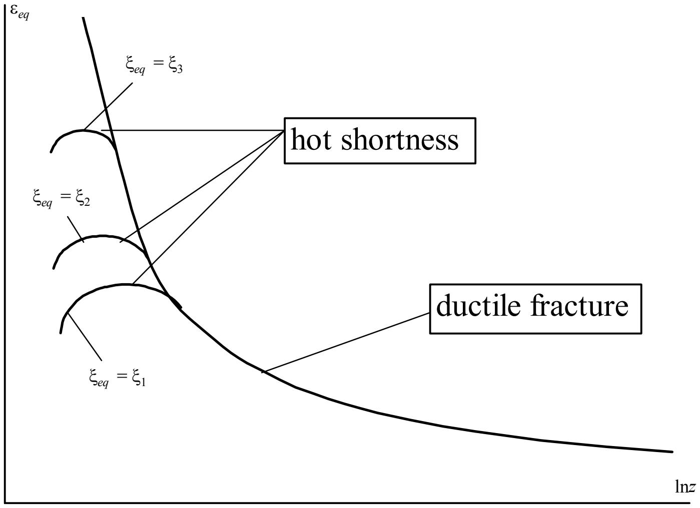

Figure 13. Schematic fracture criteria for Al-Mg alloys, where β = const showing the regimes of ductile fracture and hot shortness modes ($\xi 1 > \xi 2 > \xi 3$).

Guided by the schematic shown in Figure 13, we propose a fracture criterion for elevated temperature processing, φ_f^i, as a function of stress triaxiality, strain rate, temperature, internal state variables (S^r), and composition variables (C^r).

$$\varphi_f^i = f^i(\beta, \dot{\bar{\varepsilon}}, T, s^r, c^r) \tag{5}$$

where i represents the mode of fracture (ductile or hot shortness), β the stress triaxiality factor defined by $\beta = \sigma_h / \bar{\sigma}$, and σ_h the hydrostatic stress component, . φ_f^i is

equivalent to the effective strain at fracture $\bar{\varepsilon}_f$, and can be quantified from simplified deformation histories such as tension, torsion and compression tests.
The strain path quantity can be defined as:

$$\varepsilon_{eq} = \int_0^t \dot{\varepsilon}_{eq} dt \tag{6}$$

where $\dot{\varepsilon}_{eq} = \sqrt{(2/3)\dot{\varepsilon}_{ij}\dot{\varepsilon}^{ij}}$, $\dot{\varepsilon}_{ij}$ are the strain rate components, t is the time, and the integral should be taken over the strain path. We also introduce an average value of β over the strain path by:

$$\bar{\beta} = \varepsilon_{eq}^{-1}\int_0^t \beta \dot{\varepsilon}_{eq} dt \tag{7}$$

In the case of simple tests (uniaxial tension, uniaxial compression, and pure torsion), the values of β and $\bar{\beta}$ coincide and are determined as -1, 1 and 0 accordingly.

Assuming s^r and c^r are kept as constants, the multiple-mode fracture criterion of an Al-Mg alloy is proposed as

$$\varphi_f = \bar{\varepsilon}_f = \begin{cases} f^D\left(\bar{\beta}, \ln z\right) & \ln z \geq \ln z^{(0)}\left(\dot{\varepsilon}_{eq}\right) \\ f^S\left(\bar{\beta}, \ln z, \dot{\varepsilon}_{eq}\right) & \ln z < \ln z^{(0)}\left(\dot{\varepsilon}_{eq}\right) \end{cases} \tag{8}$$

where f^D and f^S represent fracture criteria for ductile fracture and hot shortness modes respectively.

To incorporate both stress triaxiality and LnZ, and tensile responses from Figures 9 and 10, eq. (8) can be fit to the form

$$\bar{\varepsilon}_f = \frac{2}{\left(1+\bar{\beta}\right)}\begin{cases} -3.614 + 5.680E^{-1}\ln z - 2.330E^{-2}\ln^2 z + 2.870E^{-4}\ln^3 z, & \mathrm{lnz} \geq \mathrm{lnz}^{(0)} \\ \varepsilon_0\left(\ln z - \ln z^{(c)}\right)\left(\ln z - \ln z^{(x)}\right), & \mathrm{lnz}^{(c)} \leq \mathrm{lnz} \leq \mathrm{lnz}^{(0)} \end{cases} \tag{9}$$

where ε_0, $\mathrm{lnz}^{(c)}$, and $\mathrm{lnz}^{(x)}$ are material constants.

A three dimension plot of the multiple mode fracture criterion, eq. (9), for Alloy 3 under the strain rate of 3.0/s is shown in Figure 14.

When material reaches a particular temperature, most likely above the melt temperature of a soluble phase, the matrix strength should drop significantly. In this study however, we found that the transition to failure could happen earlier (below 0.88 T_m). This transition could be influenced by strain rate, pre-strain, and alloy contents as shown in Figures 8, 9 and 10.

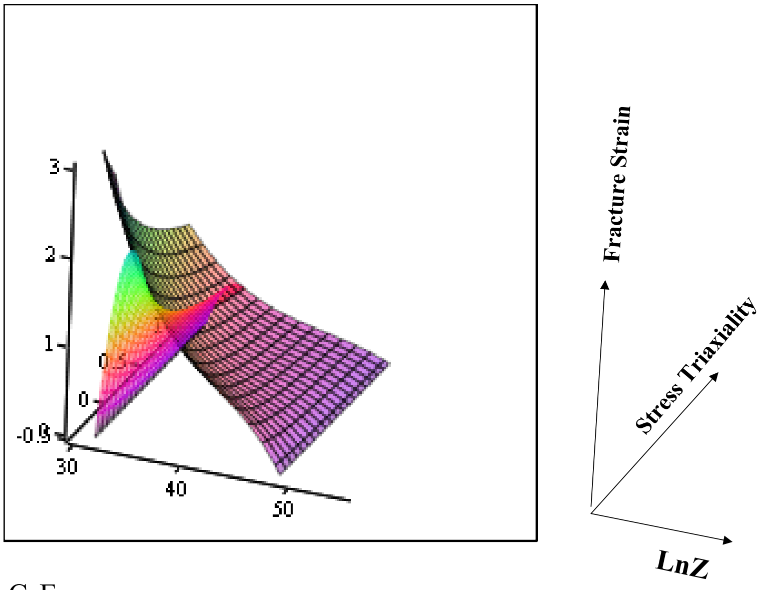

C, E

Figure 14. A three dimensional plot of fracture criterion of Alloy 3 in terms of stress triaxiality, LnZ and strain rate (0.3/s in this case) to represent both ductile fracture and hot shortness modes

The effect of prior processing is illustrated by tensile results of Alloys 2 and 3, in which the fracture strain of the latter is actually higher than the former. This could be attributed to the difference in cast porosity, since alloy 2 (as cast) may have a higher level of cast porosity than alloy 3 (partially rolled). By comparing fracture strain responses of Alloy 1 and Alloy 2, it is evident that the content of the alloy content (Mg) has significant impact on the fracture response. In the ductile fracture range, the strain to failure for Alloy 1 varies from 0.05 to 0.225, while the range for Alloy 2 is 0.2 to 0.5. For the hot shortness mode, Alloy 2 reaches the transition at between 0.85 to 0.88 T_m at the higher strain rate while Alloy 1 shows no sign of transition at these conditions.

The microstructure of Al-Mg alloys consists of constituent particles and dispersoids. The constituents are $FeAl_3$, $(Mn,Fe)Al_6$, and Mg_2Si phases and are several microns in size. They are formed during the solidification process, and are situated mainly along grain boundaries and with some dispersed in the matrix. It was found from the microstructure examination that fracture may occur by linking voids at the broken constituent particles. For the ductile fracture mode, the fracture path follows the alignment of the particles. At higher temperatures and higher strain rates, particularly for the hot shortness mode, fracture is likely still initiated at the particle sites. However, the fracture path may spread along the grain boundaries since grain boundaries are weakened. Therefore, the resulting fracture is accompanied by a different mode of strain localization. Recrystallization patches observed in the high Mg alloy (Alloy 3) may further complicate the fracture process.

Dynamic recovery may operate during deformation, leading to the replacement of the original grains by subgrains and recrystallized grains, depending on the deformation temperature, strain rate and the resulting stored energy (see Figure 11). The samples were not quenched at the end of testing, so we do not know whether subgrains and recrystallized grains were formed before or after fracture occurred. New grains formed during deformation could isolate or slow down the fracture processes. Additional research is necessary to sort out the effects of pre-processing and the grain.

3.2 NUMERICAL SIMULATIONS

Modeling of the multi-pass hot rolling process requires knowledge of several technical aspects: constitutive models for the material, thermal properties, thermal boundary conditions, interface heat conduction and interface friction. Because the large deformation and stress and temperature gradients encountered in the slab can lead to failure, fracture models are also necessary.

The computer simulations required for full 3-D, thermo-mechanically coupled analyses are lengthy, and numerical studies integrating these models are often limited. Usually, reduced two-dimensional or steady state simulations are done instead. Although analyses based on 2D models and steady state models are satisfactory for many problems, the 3D and transient nature of the problems encountered in rolling processes such as slab bulge behavior [8], center and surface inhomogeneous appearance would require 3D transient models.

With the advent of ever-increasing computer power and larger memory, large-scale rolling process models which require significant computational resources are becoming tractable using moderately sized parallel computer systems. The goals of this work are to predict temperature, strain rate, and damage evolution within the work-piece as it evolves through the multi-pass rolling process, and to determine the effect of the initial slab shape and rolling pass schedule on fracture and internal product integrity.

Extensive simulations were performed on a commercial laboratory and rolling mill configurations for a number of initial ingot side profiles including regular and irregular shapes. The constitutive and fracture models were formulated based on extensive experiments at different strain rates and elevated temperatures. The models were implemented in the LLNL finite element code ALE3D, and verification of the implementation performed. The models were further modified to meet requirements for fracture behavior at acute notch root of ingot.

3.2.1. The Model

Modeling has been established as a valuable tool for the design and optimization of metal forming processes. Many optimization problems require large-scale numerical simulations which are currently only tractable when run on moderately sized parallel computer systems. Commercially available packages capapble of running 3-D rolling process simulations are not sufficiently scalable to take advange of available parallel computational resources. The ALE3D (Arbtrary Lagrangian and Eulerian) finite element code developed at Lawrence Livermore National Laboratory is scalable on massively parallel computer platforms, and capable of running processing simulations using up to thousands of processors. This program is capable of performing simulations for elastic visco-plastic deformation combined with chemistry and heat transfer models. It runs on many platforms including IBM, Compaq, HP, Sun, Linux and Windows. The objective is to develop a numerical modeling capability, using ALE3D, to optimize the hot rolling process to minimize product loss.

The finite element model ALE3D utilizing staggered thermo-mechanical coupling was used to simulate a hot rolling process through a reversing mill. The work focuses on validation of slab shape evolution for a complete pass schedule (13 passes) by comparing with experimental results. To account for deformation and heat transfer, a staggered thermo-mechanically coupled strategy is employed. The time integration scheme adopted for the mechanical calculation is explicit with mass scaling, while that for the heat transfer calculation is implicit. The computational cost per time step for the implicit thermal calculation is higher than for the explicit mechanical calculations. Since larger time steps can be employed when solving the heat transfer equation, the thermal part of the simulation is solved once for every 10-20 explicit calculations in order to improve computational efficiency.

The geometry for the laboratory scale reversing mill simulations consists of top and bottom steel rolls, the run-out table and a 5xxx aluminum alloy slab as shown in Figure 15. The diameters of the top and bottom rolls are 0.5923 *m* and 0.5893 *m*. The initial dimensions of the slab are 0.1778 *m* in thickness, 0.4318 *m* in length and 0.3556 *m* in width. The initial temperature of the slab immediately emerging from furnace is 998 *K* and the rolls are initially 300 *K*.

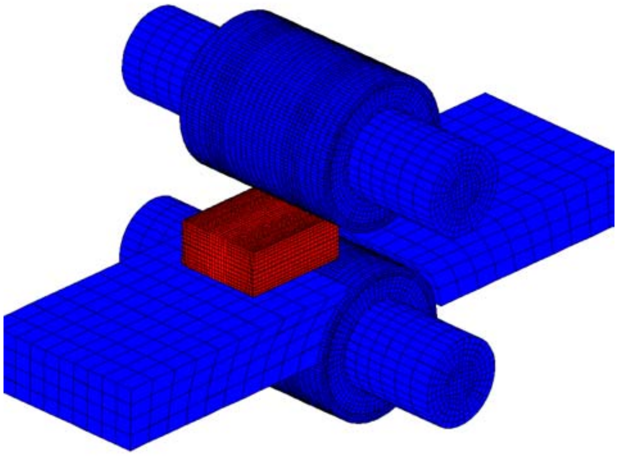

FIGURE 15. Initial Rolling geometry.

3.2.2. Heat Transfer Coefficient

The heat transfer coefficient between the roll and the slab can largely depend on specific rolling conditions such as roll speed and geometry, reduction, contact time and material [8]. Thermal boundary conditions used in the simulation include conductance at contact region and convection to the air and coolant as schematically shown in Figure 3. The interface heat transfer coefficient used in the simulations is estimated in accordance with experimental data using the laboratory mill. The specific heat, thermal conductivity and density of the 5xxx aluminum alloy were obtained from Reference [9].

A textbook value $h \sim 10\ W/(m^2 - {}^oK)$ is assumed for the convection coefficient to air. Thermal diffusion occurs continuously. An iterative trial-and-error method is employed to estimate the interface heat transfer coefficient (h) for the reversing mill experiments. The value we found for h is 150 $W/(m^2 - {}^oK)$.

At the end of each pass, the direction of the slab is reversed, and the rolls repositioned for further reduction, in accordance with the pass schedule. Continuous cooling occurs by convective heat transfer while the rolls are adjusted. The temperature of the slab decreases due to convection to air and thermal conduction from the slab to the cold rolls during the pass. At intervals of 4 passes in the experiment, the slab was reheated in a furnace to maintain a suitable deformation temperature. The reheating is captured in the model by setting the slab surface temperature to a desired level and allowing enough time for a uniform temperature to be reached throughout the slab. The roll temperature is reset to ambient temperature. Since it is not known how far the coolant flows onto the slab, the net cooling effect is approximated. The deformation heating is found to be approximately a 5 to 10 degrees Celsius increase per pass. All plastic work is converted to heat in the simulations.

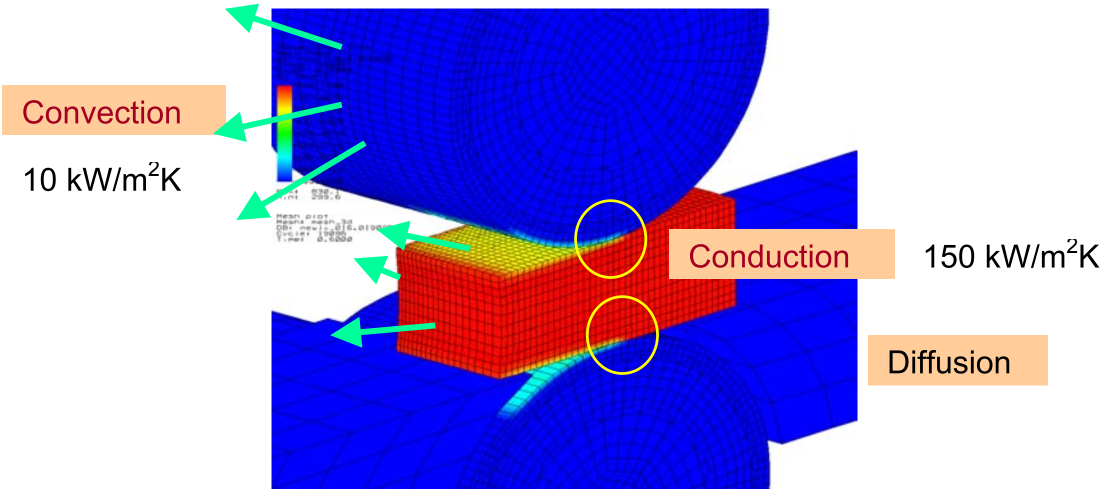

Figure 16. Thermal boundary conditions: conduction at the contact region, convection and diffusion.

3.2.3. Friction Model

The most commonly used friction model at contact interface regions is the Amontons-Coulomb friction law $\tau_f = \mu p$, where the constant of proportionality μ is the coefficient of friction [10] and p is the interface pressure. Another expression that is widely accepted for use in the metal forming industry is given by $\tau_f = m\tau_y$, where m is the friction factor and τ_y is the yield stress of the work-piece in shear. The friction model in our study is a combination of the two based on the Coulomb-type friction with a flow stress dependent maximum limit on the interfacial shear stress. It is given as:

$$\tau_f = \begin{cases} \mu p & \text{if } p < \dfrac{m}{\mu}\tau_y(\dot{\varepsilon},T) \\ m\tau_y(\dot{\varepsilon},T) & \text{if } p > \dfrac{m}{\mu}\tau_y(\dot{\varepsilon},T) \end{cases} \qquad (10)$$

Although more complex models may be necessary when conditions such as geometry and roll speed become sensitive to lubrication conditions, it is generally assumed that the value of friction factor or friction coefficient is independent of geometric constraints. Other models used in forming processes include modified versions of the Coulomb type friction model by using more complex functions of the roll pressure for the friction stress (see, for example, [11]). In our simulations, the typical values of μ and m are 0.4-0.6 and 0.8, respectively.

3.2.4. Remeshing

One important aspect noticed during the simulation is that the quality of the mesh degraded by the seventh pass, and it rapidly got worse. A more accurate representation of the deformed ingot is necessary to prevent misleading simulation results, particularly for last a few passes when element aspect ratios would be excessive. The pass schedule from Alcoa indicates that the thickness of the slab at the end of the final pass is approximately seven times smaller than the initial slab thickness. Although we have an ALE mesh capability available in our code, it will not resolve the problem because the difficulty lies in the element aspect ratio, not distortion.

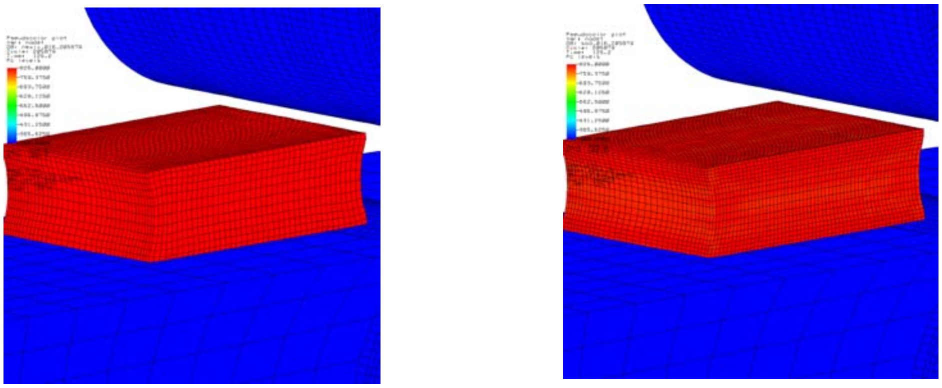

a) b)

Figure 17. a) As-deformed configuration, and b) Remapped configuration. The total number elements after remeshing increased from 8640 to 12096.

To represent the deformation more accurately, more elements should be used near the top and bottom surfaces of the slab, and more elements need to be inserted along the length as the slab lengthens. A remeshing technique has been used to create a new mesh matching the deformed geometry. Figure 17a) shows the mesh configuration of the slab after sixth pass. The re-mapped configuration is shown in Figure 17b). Values of the nodal and internal variables need to be transferred to the new mesh. An ALE3D program module called "overlink" [12] is employed to transfer the stress, state variables and temperature from the deformed configuration to the new mesh.

3.2.5. Validation against Experiment

Metrology data of the ingot profile at the end of the 8th pass was provided by Alcoa to LLNL for comparison. Detailed comparisons between the data and the initial simulation result were performed. In order to validate the integrity of the models employed, the shape change evolution of the slab was compared with experimental results. Qualitative comparison of the sectional views of the leading edge at the center plane along the length of the slab at the end of the 8th pass for both experiment and simulation is given in Figure 18-19. From the figure, it can be seen that the curvature at the slab mouth at the centerline is slightly higher than the experimental result. This may reflect mesh resolution issues where the gradient at the mid-plane is not properly resolved. Simulation results of the slab side profiles at various positions along the slab are given in Figure 20. These show good agreement with the experimental results.

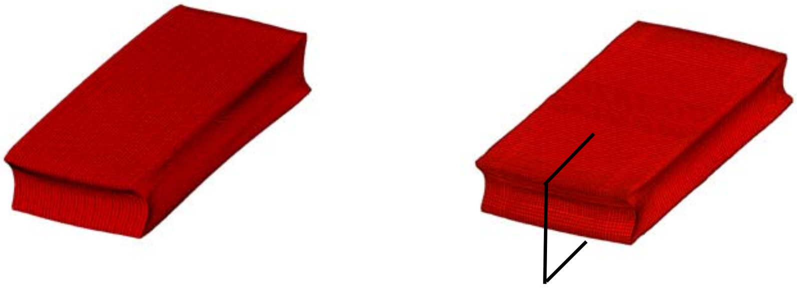
a) Experiment b) Simulation

Figure 18. Shape geometry at the end of 8th pass for a) experiment, and b) simulation


a) Experiment b) FEM Simulation

Figure 19. Sectional views of the leading edge at the center plane along the length of the slab.

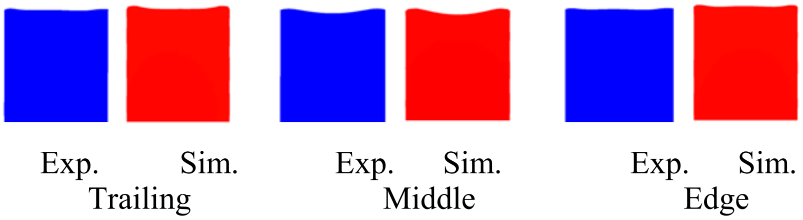

Figure 20. Side profile comparison at trailing, middle and edge plane.

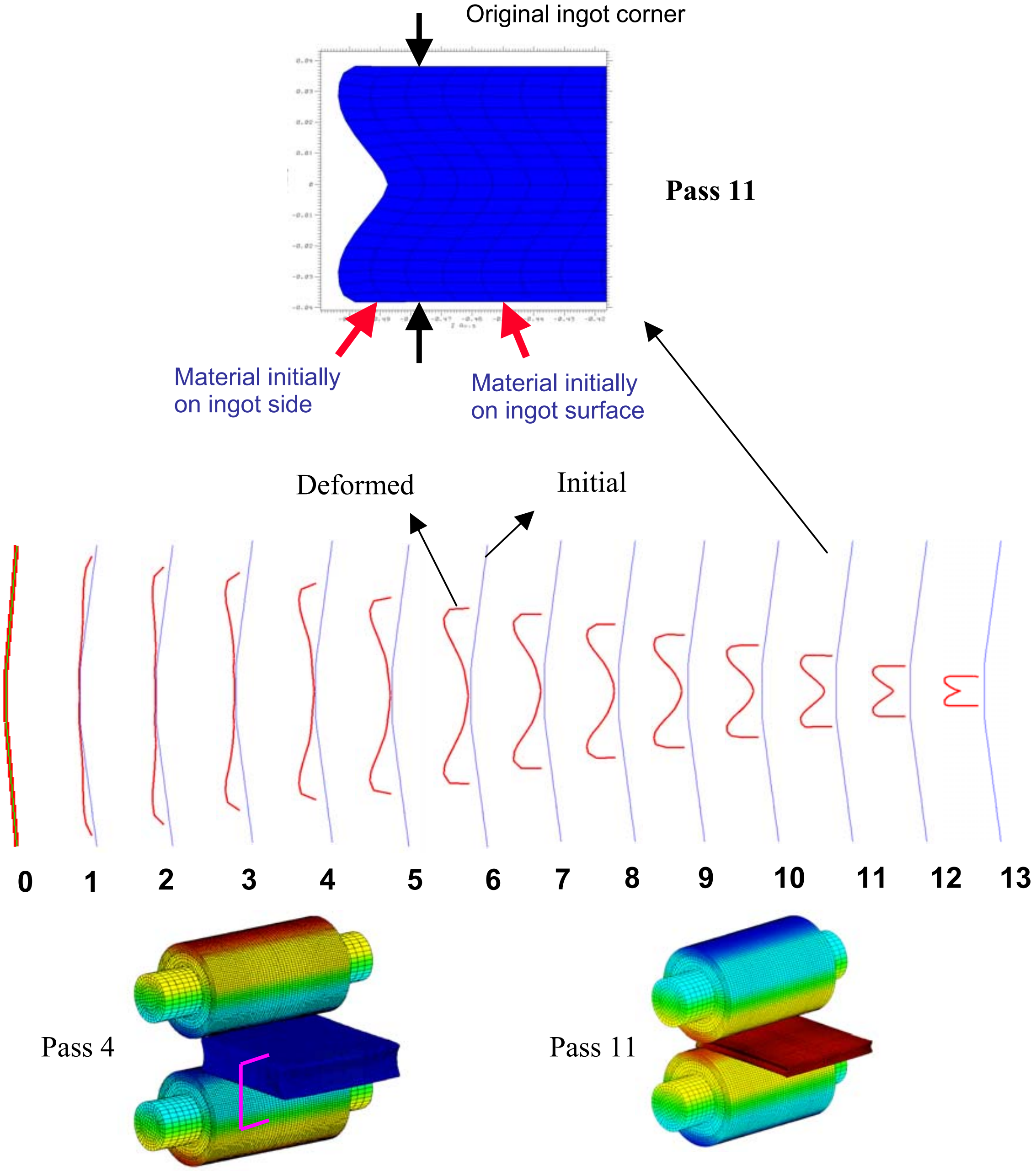

Figure 21. Slab side profile evolution up to 13th pass. Friction coefficient = 0.6.

3.2.6. Parametric Study of Friction Coefficient on Ingot Side Profile Evolution

Ingot side profile simulations were also carried out for code validation using different values of the friction coefficient. The mechanism of rollover amount of the slab is three-dimensional, which requires a moderately lengthy computer CPU time. Although the model can predict the rollover amount within a reasonable accuracy, results suggest that more simulations will lead to obtaining appropriate parameter values that would yield a correct prediction.

Simulations of the ingot shape evolution for sets of production facility mill configurations (up to 13th pass) using different friction coefficients (0.4 and 0.6) were performed to investigate the effect of friction coefficient on rollover. The simulation results shown in Figures 21 and 22 reveal that the rollover amount of the slab is strongly dependent on friction. In these plots the red line represents material that was initially on the side of the ingot. The ends of the red lines mark the original corner of the ingot. The blue line shows the location of the original ingot side compared to the current configuration. Both rollover and lateral spread are evident. Quantitative comparison suggests that the rollover amount with the friction coefficient of 0.6 at the end of the 13th pass is larger than with 0.4.

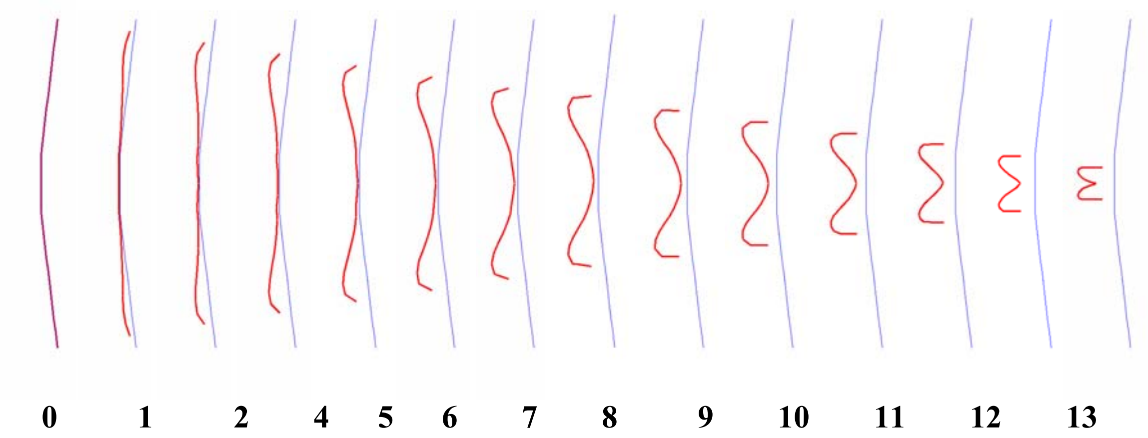

Figure 22. Slab side profile evolution. Friction coefficient used in the simulation is 0.4.

3.2.7. Alcoa Fracture Model

The failure model (Eq. 9 in Section 3.1.5) was implemented into ALE3D to capture the "alligatoring" phenomenon during the rolling process. The fracture criterion used in this model is based on the logarithm of the Zener-Hollomon parameter (thermal activation energy and temperature), strain rate, and stress triaxiality. As describe in Section 3.1.5, the model consists of two main modes of fracture: a) ductile fracture dealing with high strain rates and moderate temperature, and b) hot shortness mode for relatively low strain rates and high temperature. The model is valid for the strain rate range between 0.3 and 3.0, where the experiments were conducted, and potentially some amount of either side of this range.

FEM simulations were carried out to validate the failure model. A snapshot of the damage contour on the center plane of the slab during the 10th pass is shown in Figure 23. Although the elements at the surface have a higher magnitude of compressive stress, damage by void growth is dominated by tensile pressure at the center region. At high reductions, the pressure at the center region of the slab is compressive when in the roll bite and becomes tensile upon leaving the bite region. This changes the value of the stress triaxiality dramatically. As shown in the figure, fracture is predicted at inside center region where the pressure becomes tensile. The figure also shows that fracture at the center of the mouth at both ends of the slab is not captured. Further analysis was performed to investigate the difficulty in predicting fracture at the slab ends. The stress concentration created by the notch geometry at the slab ends can accelerate damage and promote fracture at the relatively low strain rates that exist when the notch region is not directly in the roll bite. However, the phenomenological fracture model described in Section 3.1 was calibrated for strain rates characteristic of the rolling process zone and hydrostatic stress states less severe than the leading edge notch. It was concluded that more experiments may be necessary to cover a wider range of strain rates.

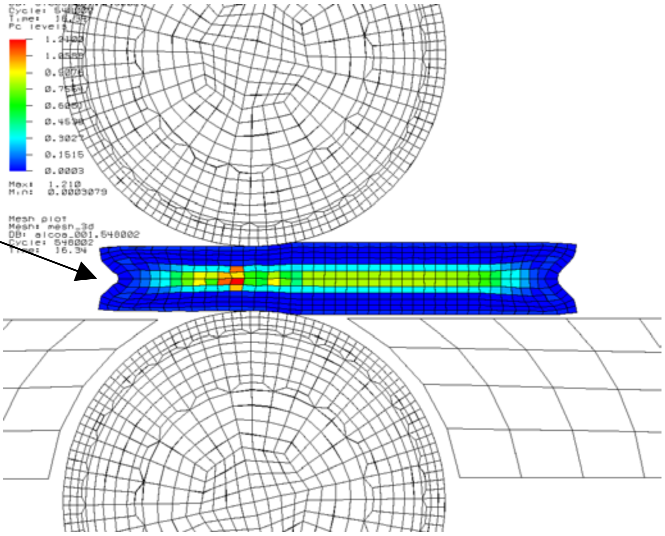

Contours of damaged material did not show expected elevation at leading edge

Figure 23. A snapshot of the damage contour on the center plane (2D cut) during the 10th pass. Fracture occurred at the center region of the slab.

3.2.8. Johnson-Cook Fracture Model

Due to the poor predictions of the experimentally-based fracture model described in Section 3.1, another type of failure model was attempted. An FEM simulation was carried out to evaluate the Johnson-Cook failure model for prediction of alligatoring. The model specifies a failure strain as a function of stress triaxiality, strain rate and temperature and given as

$$\varepsilon_f = A_1 + A_2 \exp\left(A_3 \frac{p}{\sigma}\right)\left(1 + A_4 \ln\left(\frac{\dot{\varepsilon}}{\dot{\varepsilon}_o}\right)\right)\left[1 + A_5\left(\frac{T - T_{room}}{T_{melt} - T_{room}}\right)^M\right], \qquad (10)$$

where A_1, A_2, A_3, A_4 and M are material dependent constants

This model is less sensitive to strain rate than the model described in Section 3.1 and the exponential dependence on pressure makes it more sensitive to stress triaxiality. Since the fracture is typically initiated by high stress concentration at a sharp notch, capturing the correct notch geometry at the center of the slab center, giving a higher stress triaxiality, becomes important. In simulations with the Johnson-Cook model, fracture occurs at the notch region owing to crack-like geometry that gives high stress concentration at the notch tip as shown in Figure 24a). As the slab is continuously moved to the right, the fracture propagates similar to mode I type crack as shown in Figure 24b). Snapshots of a fractured (or “alligatored”) slab and a simulation are given in Figure 25. Both experimental and simulation results show similar behavior.

The stress state before fracture is a combination of high stress tiraxiality and tensile mode stress in the vertical direction, which subsequently introduces damage accumulation near the sharp notch. One can then perform a series of simulations to obtain a relationship between reduction and fracture initiation and establish a pass schedule that would yield a larger reduction, with better quality, without any occurrence of fracture.

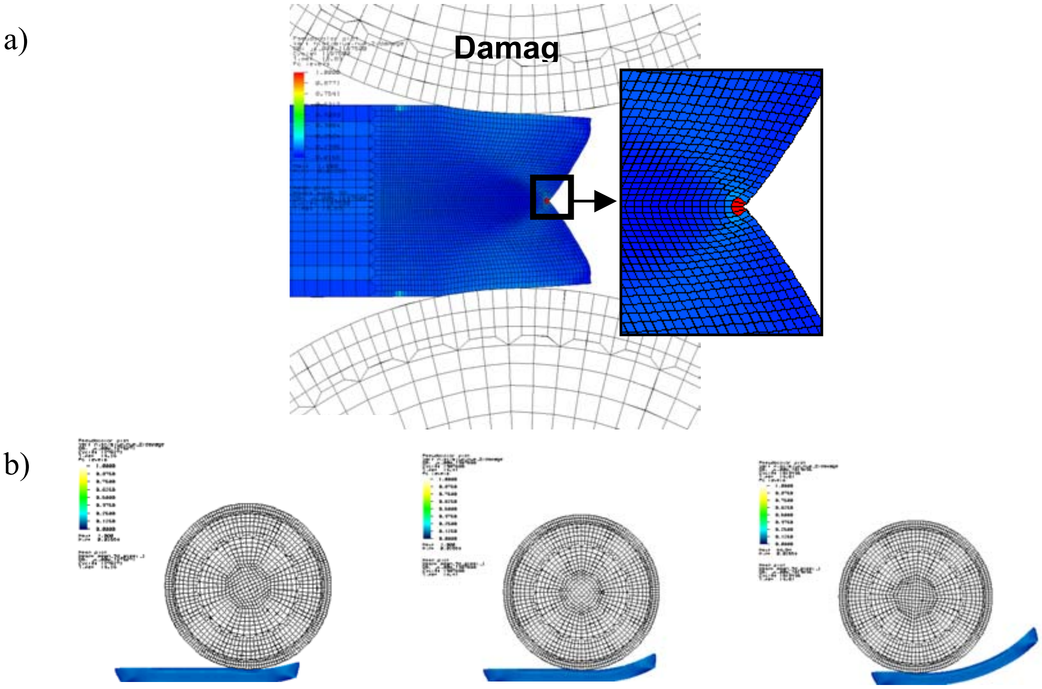

Figure 24. a) Damage at notch region (indicated by red color) and b) snapshots of fractured ingot.

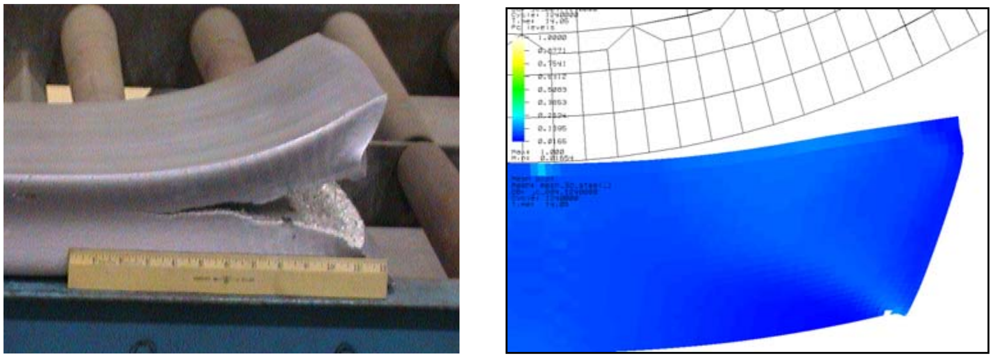

a) b)

Figure 25. a) Fractured ingot and b) simulation of center splitting

3.2.9. Code Performance

The simulations were run on many existing computational resources at LLNL which include a combination of personal computers, workstations and mainframe architectures, including massively parallel systems. Since the problem size is suitable for only a small cluster of several workstations, most simulations were run using less than 64 processors on a Linux cluster with 2.4 GHz processors with a small memory size. Figure 26 shows parallel scaling of the simulations, where a speed up of 8 using 10 processors was achieved for an 82960 element sized problem.

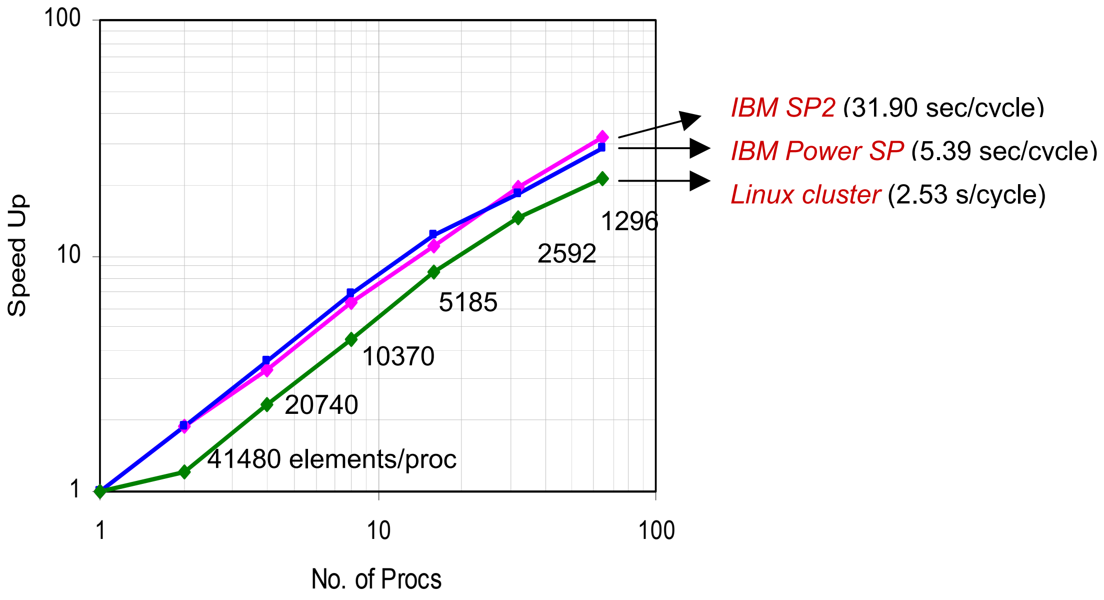

Figure 26. Speed up vs. number of processors

4. CONCLUSION

Numerical modeling capabilities for optimization of reverse multi-pass hot rolling processes have been successfully developed at Lawrence Livermore National Laboratory (LLNL) under a joint CRADA project with the Alcoa Technical Center (ATC) sponsored by the DOE Office of Industrial Technologies. This tool will be used in the design of forming processes to minimize the loss of product and eliminate the energy waste associated with recycling scraped product. The modeling capability developed by the project partners will also be used to produce plate more efficiently and with better properties.

5. COMMERCIAL APPLICATION

Commercial application will proceed at Alcoa by using the software to optimize ingot shape and pass schedules. Ingot shape changes will reduce edge cracking and rollover on edges and ends. Pass schedule modifications may permit a greater reduction without alligatoring. The software has been installed at the Alcoa Technical Center. It is expected that the ATC will perform the optimization calculations as a service to the rolling plants. Both rollover and fracture will be used as design criteria. LLNL will provide updated versions of the code and support. Calculations using a few production ingot geometries and mill configurations have been run at LLNL. The presentation of these results by Ming Li at a meeting of Alcoa rolling plant managers was well received, and several plants have expressed interest in application as soon as possible. This design tool will support Alcoa’s near term efforts to optimize ingot profiles at 30 plants worldwide. The Alcoa Technical Center will perform analysis of production environments at its rolling plants to produce better design guidance for use at the production plants.

LLNL and Alcoa are continuing to explore other technical areas for future collaborations.

REFERENCES

1. J. K. McBride, R. E. Sanders, Jr. and H. G. Reavis, "The Development of 5xxx Alloys for RCS Applications," *Journal of Metals*, 18-21 (1996).
2. Ashby, M.F., Gandhi, C., and Taplin, D.M.R., "Fracture-Mechanism Maps and Their Construction for F.C.C. Metals and Alloys", Acta Metallurgica, **27**, pp. 699-729.
3. Sample, V.M. and Lalli, L.A., Material Science and Technology, **3**, 28-35 (1987).
4. Wang, P.T. and Richmond, O., "Overview of a two state variable constitutive model for the consolidation and forming processes of powder-based porous metals," ASME annual meeting, Mechanics of Granular Materials and Power Systems, Editor: M.M. Mehrabadi, Book No. G00742, MD-Vol. **37**, 63-83 (1992).
5. Vujovic, V. and Shabaik, A.H., "A New Workability Criterion for Ductile Metals", *Trans. ASME J. Engn Mater. Struct.*, **108**, 245–249 (1986).
6. Alexandrov, S., Chicanova, N. and Vilotic, D. Compression of a Block Between Cylindrical Dies and its Application to the Workability Diagram. In: *Proc. 3rd Int. Conf. on Materials Processing Defects "Advanced Methods in Materials Processing Defects"* (Eds M. Predeleanu and P. Gilormini), Elsevier, Amsterdam, 247-256 (1997).
7. Vilotic, D., Chikanova, N. and Alexandrov, S.,"Disk Upsetting Between Spherical Dies and its Application to the Determination of Forming Limit Curves", *J. of Strain Analysis*, **34**, 17-22 (1999).
8. Lee, Y and Dawson, P, "Buldge Predictions in Steady State Bar Rolling Processes", *Int. J. for Num. Methods in Engng.,* **30**, 1403-1413 (1990).
9. Tseng, A.A., "Thermal Modeling of Roll and Strip Interface in Rolling Process: Part2-Simulation", *Numerical Heat Transfer, Part A*, **35**, 115-133 (1999).
10. H. Boyer and T. Gall, *"Metals Handbook"* Desk Edition, American Society for Metals, Metals Park, Ohio (1985).
11. Keife, H. and Sjogren, C., "A Friction Model Applied in the Cold Rolling of Aluminum Strips", *Wear*, **179**, 137-142 (1994).
12. ALE3D, Lawrence Livermore National Laboratory, (2003).